Binding and Orientation of Carbamate Pesticides on Silica Surfaces

Leander Bromley III,[a§] *Pablo E. Videla,* [b§] *Jerry L. Cartagena-Brigantty,*[a]

Victor S. Batista,[b*] *Luis Velarde*[a*]

[a]*Department of Chemistry, University at Buffalo, State University of New York, Buffalo, New York 14260-3000, United States*

[b]*Department of Chemistry, Yale University, New Haven, Connecticut 06520, United States*

§ L.B. and P.E.V. contributed equally to this work.

Corresponding Authors

*Email: victor.batista@yale.edu; lvelarde@buffalo.edu;

Abstract

Carbaryl (1-naphthyl-N-methyl carbamate) is one of the most abundantly used carbamate pesticides and a common ground and surface water contaminant. Despite this, there is a lack of understanding regarding the specific interactions between this pesticide and mineral particles with environmental impact, including soil and dust aerosol interfaces. Here, we examine the adsorption of carbaryl to hydrophilic silica surfaces by applying a combination of vibrational Sum Frequency Generation (vSFG) spectroscopy and atomistic simulations. We find that carbaryl molecules readily adsorb to silica/air interfaces by hydrogen bonding interactions between the carbamate group (primarily the -NH terminus, secondarily the ester -C=O ester moiety) and the surface silanols and silenolates. On average, this results in the naphthyl aromatic ring being oriented roughly parallel to the surface. Our characterization of interactions of carbamate pesticides at silica surfaces is particularly valuable for understanding transport, stabilization, and potential degradation mechanisms of carbamate pesticides by interfaces during downstream processes of environmental relevance.

TOC GRAPHICS

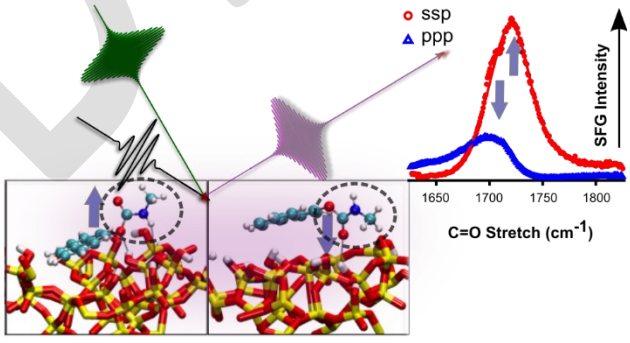

INTRODUCTION

Approximately 5.6 billion pounds of pesticides are used globally every year.[1] Organonitrogen pesticides (ONPs) occur widely in the environment and are persistent in aquatic systems,[2] including the carbamate pesticide family of compounds which consist of esters derived from carbamic acid (NH_2COOH), with the general formula R-NHCOO-R'. Here, we focus on carbaryl (***Figure 1***) a carbamate introduced in the late 1950s and currently the third most used home and garden pesticide in the United States.[3] In commercial products such as Sevin and Dicarbam, carbaryl is extensively applied in agriculture and in commercial and household settings.[3, 4] With increased application over the past decades, this pesticide increasingly poses environmental and health risks via contamination of ground and surface water. Carbaryl is reported as the second most frequently found insecticide in groundwaters.[5] It's presence has been detected in rain runoff at 1737 ppb,[6] and studies have confirmed the incidence of carbaryl and/or its hydrolyzed products in soils at 16.3 ppm.[7]

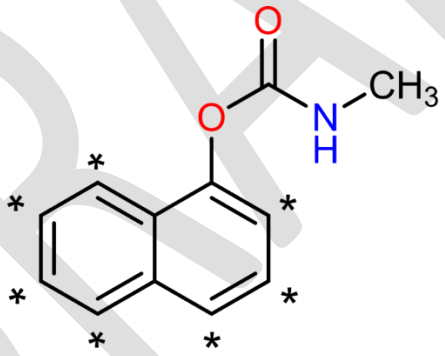

Figure 1. Molecular structure of carbaryl (1-naphthyl-N-methyl carbamate). Each asterisk represents a hydrogen atom (substituted with deuterium in the partially deuterated carbaryl-d7).

Several studies have focused on the toxicity and environmental effects of the carbaryl pesticide family in various environmental compartments. However, a molecular level understanding of interactions of these pesticides at mineral surfaces remains to be established.[8-11] Those interfacial interactions are critical for accumulation, transport, and degradation during downstream processes of environmental impact,[12, 13] as they play an active role in the reactivity and mobility of pesticides in the environment.[14-17] It is therefore essential to develop a fundamental, atomistic understanding to determine how these processes are regulated by molecule-surface interactions.[18-20] Silica/quartz

is one of the most abundant primary minerals in most types of soils and mineral aerosols,[21] therefore it is an ideal model substrate to investigate the properties of carbaryl adsorbates. For instance, a recent study showed that upon solar light exposure of carbaryl on silica, among their soil models, the quantum yield of disappearance was about one order of magnitude higher than that in aqueous solution.[22]

Here, we primarily focus on the interfacial structure and the surface anchoring mechanism of carbaryl on silica using a combination of surface-selective nonlinear vibrational spectroscopy and computational modeling, including molecular dynamics simulations and *ab initio* calculations of vibrational spectra. Raman and Fourier Transform Infrared (FTIR) vibrational spectroscopic methods have been widely applied to study pesticides in bulk solutions and films.[9, 23-27] Here, we apply vibrational sum frequency generation (vSFG) spectroscopy, an *in-situ* technique particularly suitable for the analysis of molecules at buried interfaces and sensitive to sub-monolayer amounts of adsorbates.[14, 16, 28-33] As a coherent non-linear spectroscopic technique, the vSFG response is highly sensitive to molecular orientation and ordering at the surface.[34, 35] Making vSFG a powerful technique for obtaining detailed chemical information regarding the molecular composition, structure, and interactions of molecules at interfaces. As such, it has become a versatile tool for studies of environmental surfaces and interfaces under ambient conditions,[14, 29, 36-39] and for revealing structure–activity relationships of surface-immobilized compounds, like antimicrobial coatings.[40-43]

In this work, we analyze the vSFG spectra of carbaryl at air/silica interfaces by using molecular dynamics (MD) simulations, density functional theory (DFT) calculations, and calculations of vSFG spectra.[44-54] The resulting analysis provides detailed structural and orientational information of carbaryl on the silica surface. Our spectral peak assignments and molecular orientation are validated by using phase-resolved vSFG measurements and simulations.[55] Our findings reveal that carbaryl adopts a dominant conformation at the silica/air interface preferentially anchored by hydrogen bonding interactions between the carbamate group (primarily the -NH terminus) and the surface silanolates/silenols ($Si–O^-$/Si–OH). The naphthyl aromatic ring is oriented nearly parallel to the surface in close contact with the silica surface. The resulting characterization level is particularly relevant to studies of carbamate pesticides of environmental impact focused on the nature of molecular stabilization by interaction with mineral surfaces and potential degradation mechanisms.

EXPERIMENTAL AND COMPUTATIONAL METHODS

Sample Preparation. 1-naphthyl-N-methyl carbamate or carbaryl was purchased from Sigma-Aldrich (≥98.0%). The pesticide was used as received and dissolved in HPLC grade acetonitrile (Fisher Chemical, >99.9%) to a concentration of 5.0 mM via serial dilution.

A fused quartz microscope slide (Electron Microscopy Sciences) was carefully cleaned and dried before a two-drop aliquot of the 5.0 mM Carbaryl solution was deposited onto the substrate (ca. 6.5 cm^2) and homogenized via spin-coating at 3000 rpm for 30 seconds to evaporate the organic solvent. The resulting films exhibited good homogeneity after solvent evaporation and consistent vSFG results were obtained for solutions below 5.0 mM, spectral lineshape differences were observed for higher concentrations (see the SI). The use of spin-coating deposition with ≤5 mM concentration provided stable samples even for the longer acquisitions required for good signal to noise ratios (*vide infra*). Below 1.0 mM, however, the films generated very weak vSFG signals using this method. Besides the consistency of the films, acetonitrile was used in this work to keep carbaryl a neutral molecule and the silica surface unaffected after solvent exposure,[14] allowing for direct comparison with theory. While environmentally relevant, adsorption experiments from an aqueous solution are out of the scope of this article and the focus of separate future work. For spectral assignments, we used partially deuterated carbaryl-d_7 (98 atom % D) as received from CDN Isotopes. The carbaryl-d_7 sample was prepared following the exact same sample preparation procedure as described above for carbaryl.

A similar sample preparation procedure was employed for phase-resolved vSFG experiments. A two-drop aliquot of 1.25 mM solution of carbaryl dissolved in HPLC-grade acetonitrile was deposited on a freshly cleaned z-cut α-crystalline quartz window with dimensions of 12.7 x 12.7 x 5 mm^3, purchased from CASTECH INC (Fuzhou, China), via Pasteur pipette and homogenized via spin-coating at 3000 rpm for 30 seconds. The crystalline quartz window was cleaned by wiping it with a Kimwipe (Kimtech Science) soaked in methanol (HPLC grade, Fisher Chemical) followed by soaking it in freshly prepared NOCHROMIX (Godax Laboratories Incorporated) solution for 1 minute and then rinsed with copious amounts of ultrapure water. The quartz window was then dried under ultrapure nitrogen flow, followed by ultraviolet-ozone treatment for 1 hour.

VSFG Spectroscopy. In brief, vSFG is based on a second-order process where two ultrafast laser pulses are temporally and spatially overlapped at the sample interface to produce a third pulse, which oscillates with the sum frequency.[30, 38, 56, 57] One of the two incident beams has infrared frequency (ω_{IR}) while the other involves visible light (ω_{Vis}). The generated signal beam has a frequency equal to the sum of the frequencies of the two incident pulses ($\omega_{SFG} = \omega_{IR} + \omega_{Vis}$) and it is resonantly enhanced when the infrared frequency ω_{IR} excites a vibrational mode of a molecule at an interface. A lack of inversion symmetry is required for signal generation in SFG spectroscopy, so the technique is inherently interface selective.[30, 34, 57-59] The sum frequency experiments were conducted using a customized broadband vSFG spectrometer,[60] which has been previously described elsewhere.[61-64] A regeneratively amplified Ti:Sapphire laser (Legend Elite HE+, Coherent Incorporated) produces ultrafast laser pulses (~35 fs) at a 1 kHz repetition rate and a center wavelength of 800 nm. The amplifier output is subsequently split to pump an optical parametric amplifier (TOPAS Prime, Light Conversion) followed by a noncollinear difference frequency generator (NDFG) which generates tunable, mid-IR, broadband pulses with a bandwidth of approximately 400 cm^{-1} utilizing a $AgGaS_2$ crystal. The second portion pumps a second harmonic bandwidth compressor (SHBC, Light Conversion) which produces narrowband 400 nm light with a pulse duration of ~5 ps and a bandwidth of ~7 cm^{-1}. The 400 nm pulse is used as a pump for a picosecond optical parametric amplifier (TOPAS-400-WL, Light Conversion) that generates continuously tunable, narrowband, visible-frequency pulses. For this study, the visible pulse wavelength is held at 660 nm, energetically away from any electronic resonances. The visible and IR beams overlapped, spatially and temporally, at the sample surface with incidence angles of 45° and 70°, respectively, relative to the surface normal. The vSFG beam was guided into a spectrograph (Acton SP2500, Princeton Instruments) equipped with a liquid nitrogen cooled CCD camera (PYL100BRX, Princeton Instruments). Integration times for signal acquisition ranged from 30–90 minutes per spectrum. No sample photodegradation was observed, even after several hours of exposure. We select the polarization of the SFG, visible, and IR beams to be either S or P polarized to probe a specific combination of tensor elements of the nonlinear susceptibility $\chi^{(2)}$. A polarization combination of SSP, refers to S polarized SFG beam, S polarized visible, and P polarized IR, respectively. Each spectrum, as reported below, has been background subtracted and normalized both with respect to acquisition time and intensity of the non-resonant PPP SFG signal produced by a clean polycrystalline gold film under equivalent experimental

conditions. The vibrational frequency axes of these spectra are calibrated utilizing spectra collected from the gold film after placing a polystyrene film into the path of the IR frequency beam. The entire optical path of the IR beam was enclosed and atmospheric absorption bands were minimized by flushing the housing with air from a Parker/Balston purge gas generator.

Phase-resolved vSFG. Heterodyned vSFG enables phase sensitive measurements, including extraction of the real and imaginary components of the interfacial vibrational response function proportional to the nonlinear susceptibility $\chi^{(2)}$. Phase-resolved measurements here are based on the internal heterodyne method, where a freshly cleaned z-cut α-crystalline quartz window was used as a substrate instead (see the SI).[28, 65, 66] In summary, when the vSFG spectrum of a sample on the z-cut α crystal quartz surface is measured, the vSFG response has contributions from the bulk of the z-cut α quartz crystal (internal local oscillator) and from the molecules adsorbed on the quartz crystal surface. A detailed phase-resolved SFG study by Wang et. al showed the application of the internal-heterodyne method by utilizing the azimuthal angle phase dependence of the right-handed z-cut α quartz crystal.[65, 66] In our experiment, carbaryl $I_{\pm x}^{Norm}$ SSP and PPP spectra on quartz were obtained at azimuthal angles of Φ=0° (+x axis) and Φ=180° (-x axis) by a 15 second acquisition and normalized to non-resonant response of the bare z-cut α quartz crystal under the +x direction (see the SI). The quartz-normalized effective imaginary susceptibility reported here was obtained therefore via:

$$\mathrm{Im}[\chi_{eff}^{(2)}] = \frac{I_{+x}^{Norm} - I_{-x}^{Norm}}{4} \quad (1)$$

Molecular Dynamics (MD) Simulations. MD simulations were performed for carbaryl on a model slab of amorphous silica. The silica slab used is based on previous studies,[53, 67] and corresponds to a 115×115×20 Å slab adopted from the work of Cruz et al.[68] Our model of the silica surface had a surface Si−OH concentration of 4/nm^2, within the experimental range of 2.6–4.6/nm^2.[69] The exact concentration of carbaryl adsorbates onto the silica surface is not known. We have assumed a dilute surface concentration of 0.1/nm^2 for the MD simulations. This corresponds to a total of 13 carbaryl molecules on the model slab of amorphous silica surface.

The interaction parameters for the amorphous silica were taken from Ref.[68] The force field parameters have been optimized to reproduce the water contact angle and have been successfully applied to simulate amorphous silica surfaces,[70] quartz(1011)−water interfaces,[71] and ionic transport in silica channels.[72] The initial force field parameters for the carbaryl molecules were

generated via the MATCH web server,[73] based on the CGenFF engine.[74-76] The atomic charges were obtained from the fitted restricted electrostatic potential (RESP) based on DFT calculations at the B3LYP/6-31+G(d) level of theory.[77-79] See SI for a summary of the interaction parameters.

All MD simulations were carried out using the NAMD program.[80] The carbamate molecules were randomly positioned on the hydroxylated surface using the Packmol package,[81] and the entire system was minimized for 15000 steps. The whole system was then equilibrated for 100 ps before launching a production run of 20 ns and recording the configuration snapshots every 1 ps. Simulations were performed with an integration time step of 1 fs and periodic boundary conditions at 300 K. Intermolecular van der Waals interactions were calculated with a cutoff of 12 Å (switching function starting at 10 Å). Long-range electrostatic forces were calculated using the Particle mesh Ewald (PME) summation method. The Langevin thermostat was used to maintain a constant temperature in the NVT ensemble. The elementary cell extension of the system was 115×115×115 Å where the periodicity along the z-axis was increased deliberately to create 95 Å of empty space above the surface. To keep the amorphous slab rigid, silica atoms were fixed at their minimized positions during the MD simulation.

DFT Simulations. Molecular geometry optimizations at the DFT level were performed with the Gaussian 16 software package,[82] using the B3LYP hybrid functional[77] and the 6-31+G(d) basis set.[78, 79] Harmonic frequency calculations were performed on the optimized stationary point to obtain frequencies, dipole and polarizability derivatives for each normal mode. An "ultrafine" integration grid (99 radial shells and 590 angular points per shell) was used for the frequency calculations to obtain accurate results. Additionally, anharmonic frequency calculations based on second-order perturbation theory (VPT2)[83-86] were performed to obtain coupling parameters for the inclusion of Fermi resonances (FR). All harmonic frequencies were scaled by 0.955 to facilitate the comparison with experimental spectra.

SFG spectra were simulated at the DFT level as has been previously described. [44-54] Briefly, we computed the second-order molecular hyperpolarizabilities,

$$\beta_{\alpha\beta\gamma,q} \approx \frac{\partial \alpha_{\alpha\beta}}{\partial Q_q} \frac{\partial \mu_\gamma}{\partial Q_q} \quad (2)$$

where $\alpha_{\alpha\beta}$ and μ_γ are elements of the polarizability and dipole moment in the molecular frame, and Q_q is the normal mode coordinate of the q-th vibrational mode. The hyperpolarizability was then rotated to the laboratory frame to obtain the second-order susceptibility,

$$\chi^{(2)}_{ijk,q} = \sum_{\alpha\beta\gamma} \langle R(\psi)R(\theta)R(\phi)\beta_{\alpha\beta\gamma,q} \rangle \quad (3)$$

where $R(\psi)$, $R(\theta)$, and $R(\phi)$ represent the Euler rotation matrices required to superimpose the axes of the molecular coordinate system with those of the macroscopic laboratory coordinate system. The orientation parameters, represented by the Euler angles ψ, θ, and φ, are defined by the angular displacement of each axis of the molecular coordinate system from the corresponding axis of the laboratory coordinate system. Angular brackets in equation (3) represent averages over different configurations sampled from MD simulations. The SFG intensity was then computed, as follows:

$$I_{SFG}(\omega_{IR}) = \left| \sum_k \frac{\chi^{(2)}_{eff,q}}{\omega_{IR} - \omega_q + i\Gamma_q} \right|^2 \quad (4)$$

where Γ_q= 15 cm^{-1} and the effective susceptibilities for SSP and PPP polarization are

$$\begin{aligned} \chi^{eff}_{ssp,q} &= L_{yyz}\chi^{(2)}_{yyz,q}, \\ \chi^{eff}_{ppp,q} &= L_{zxx}\chi^{(2)}_{zxx,q} + L_{zzz}\chi^{(2)}_{zzz,q} - L_{xxz}\chi^{(2)}_{xxz,q} - L_{xzx}\chi^{(2)}_{xzx,q} \end{aligned} \quad (5)$$

where the L_{ijk} terms are the Fresnel factors (listed in the SI) that depend on the refractive index of the interface as well as the incident angle of the beams.[58, 87, 88]

RESULTS AND DISCUSSIONS

C-H Stretching Region. Figure *2* shows representative vSFG intensity (or homodyne-detected) (Figure 2A and 2B) and phase-resolved (or heterodyne-detected), vibrational spectra in the C-H stretching region of carbaryl at the air/quartz interface collected *in-situ* under ambient laboratory conditions (30% relative humidity) with SSP and PPP polarization combinations. Data are representative of independent experiments performed in triplicates with similar results. The vSFG selection rules require that vibrational modes must be both Raman and IR active to be observed, so bulk Raman and IR vibrational spectra of carbaryl are provided in the SI for reference.

The SSP and PPP spectral lineshapes provide essential information to elucidate the molecular orientation by direct comparisons to DFT simulations.[30, 34, 56, 57] The SFG vibrational frequencies in the C-H region were obtained by performing a global fit of the SSP and PPP spectra assuming a Lorentzian profile for each peak (see the SI). **Table *1*** summarizes the fitting results and assignment of the major peaks indicated by arrows in Figure 2D. The vibrational mode assignments are supported by our DFT calculations (SI). The carbaryl C-H stretching assignments agree, in general, with previous vSFG studies that examined molecules with structural similarities.[14, 31, 89-91] Spectral features become better resolved in the phase resolved spectra (2C and 2D) where a phase flip between symmetric and antisymmetric stretches is clearly observed.[66]

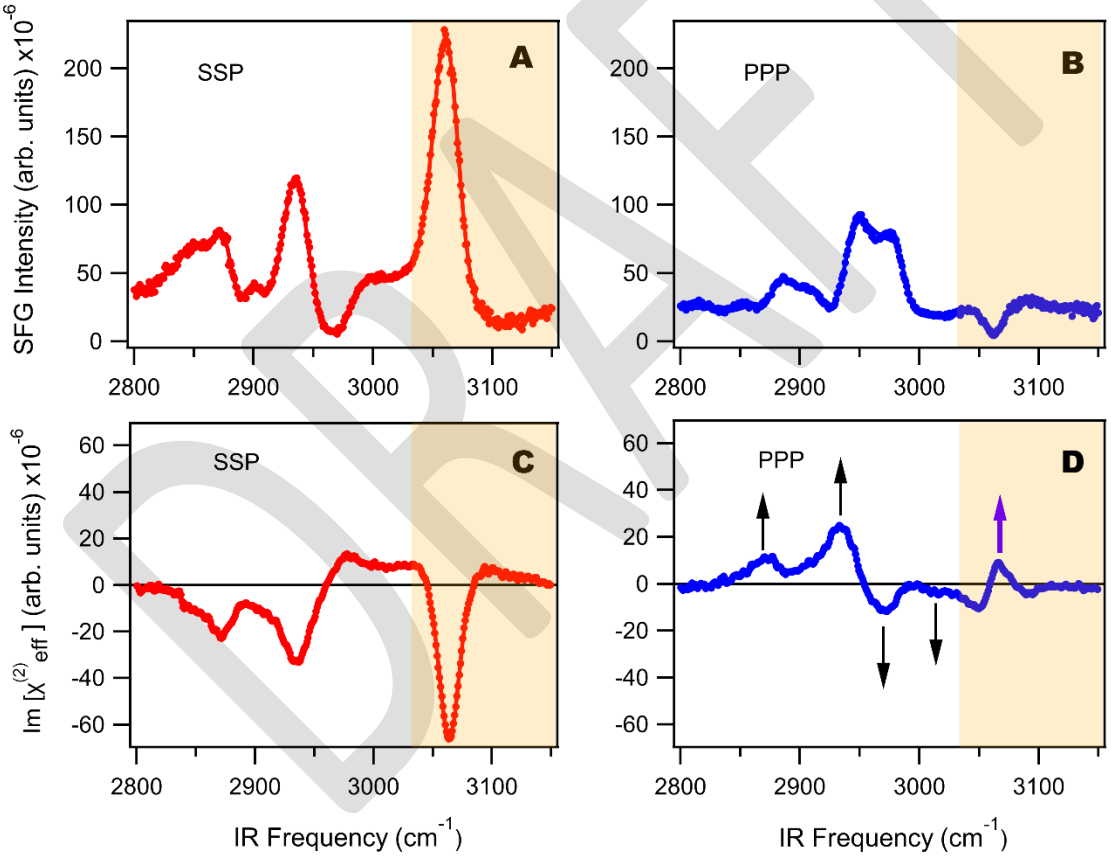

Figure 2. Normalized intensity vSFG spectra in SSP (A) and PPP (B) polarization for carbaryl on fused quartz at the solid/air interface. Phase-resolved, quartz-normalized imaginary vSFG spectra for carbaryl on z-cut alpha quartz at the solid/air interface for SSP (C) and PPP (D) polarization combinations. The dots are raw data and the solid lines are the results of the best fits. The spectra are divided (as a guide-to-the-eye) into the CH_3 stretching region at lower frequencies and the aromatic CH stretch region (shaded) at higher frequencies. The arrows in (D) represent the position and phase of the major resonances summarized in Table 1.

SSP-polarized SFG spectra probes only a single component of the nonlinear susceptibility, namely $\vec{\chi}^{(2)}_{yyz}$. On the other hand, PPP-polarized SFG spectra probes four non-linear susceptibility components, namely $\vec{\chi}^{(2)}_{xxz}, \vec{\chi}^{(2)}_{xzx}, \vec{\chi}^{(2)}_{zxx}$ and $\vec{\chi}^{(2)}_{zzz}$ (see SI). For P-polarized IR, as used in the experiment, detection of CH stretching modes requires a dynamic transition dipole moment with a component along the surface normal in order to be active.[89] It is important to note that the band at ~3055 cm-1 dominates the SSP spectrum but its intensity in the PPP spectrum is very weak. We assign this band to the aromatic C-H stretching vibration, and to confirm this, ***Figure 3*** compares intensity vSFG spectra of carbaryl and partially deuterated carbaryl-d7 (***Figure 1***). Unsurprisingly, this peak vanishes in the partially deuterated carbaryl-d7 SFG spectrum due to the absence of C-H aromatic contributions, in direct agreement with the spectral assignment and ruling out NH vibrational modes or high frequency methyl antisymmetric stretches. This dominant SSP contribution of carbaryl at ~3055 cm^{-1}, is also in agreement with the sharp resonance observed at 3057 cm^{-1} in vSFG studies of naphatalene films.[92, 93] The unique relative polarization-dependent intensity of the C-H stretching aromatic band in the carbaryl spectrum will be used to determine the orientation of the carbaryl naphthyl ring at the air/solid interface.

Another notable spectral feature includes the peak around 2930-2945 cm^{-1}, which we have assigned as a Fermi resonance. That band arises from the coupling between the CH_3 symmetric stretch fundamental (seen at 2870 cm^{-1}) and the CH_3 symmetric bending overtone, as discussed in earlier SFG studies.[31, 33, 58, 59, 94-96]

Table 1. Table summarizing the results of fits to the intensity vSFG spectra of carbaryl on fused quartz at the solid/air interface (SS = Symmetric Stretch; AS = Antisymmetric Stretch).

Vibrational Frequency (cm^{-1})	Vibrational Mode Assignment
Phase-resolved SFG	
2870.70 +/- 0.20	-N-CH_3 (SS)
2936.26 +/- 0.20	Fermi Resonance
2975.72 +/- 5.62; 3008.26 +/- 3.56	-N-CH_3 (AS)
3061.74 +/- 1.88; 3063.8 +/- 1.11	Aromatic C-H
Homodyne SFG	
2878.94 +/- 0.27	-N-CH_3 (SS)
2937.30 +/- 0.32	Fermi Resonance
2984.55 +/- 0.43	-N-CH_3 (AS)
3055.08 +/- 6.59; 3056.40 +/- 4.43	Aromatic C-H

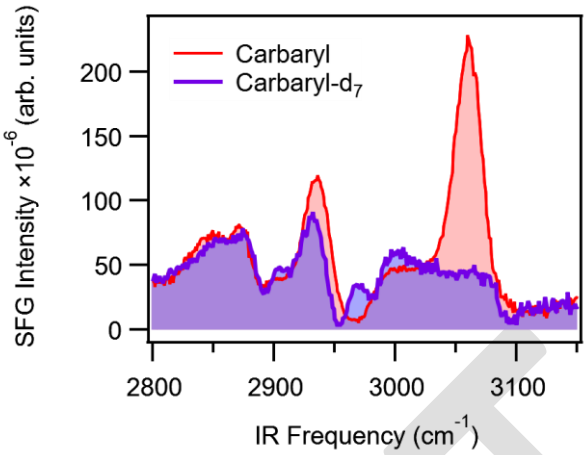

Figure 3. Homodyne-detected SFG vibrational spectra of carbaryl (red) and carbaryl-d7 (purple) on quartz at the solid/air interface. The non-vanishing contributions in carbaryl-d7 (purple) above 3000 cm^{-1} is attributed to small contributions from the higher energy antisymmetric stretch and an overtone of the carbon-carbon symmetric stretch as reported in ref.[92]

O-H/N-H Stretching Region. ***Figure 4*** shows representative spectra of the homodyne-detected vSFG experiments corresponding to the N-H/O-H stretching region, including both the bare silica substrate and the silica substrate coated with the pesticide. These experiments allow for further characterization of the binding interactions between carbaryl and the silica substrate through simultaneous detection of the O-H stretch of the silanol groups (≡SiO-H) and the N-H stretch of the pesticide carbamate group.

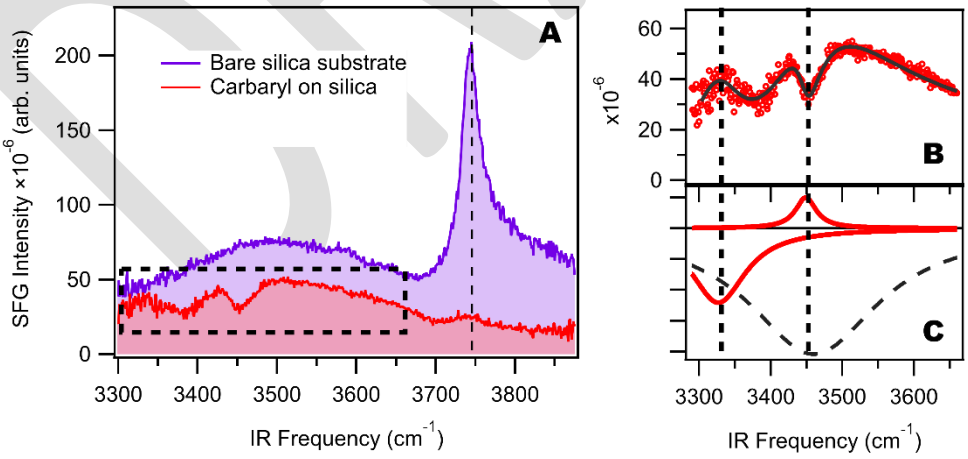

Figure 4. Representative spectra of bare silica and silica coated with carbaryl at the silica/air interface (A). The area inside the dashed rectangle in (A) is expanded (red markers) and fitted (solid line) in (B) to the three Lorentzians shown in (C) as discussed in the text.

The SFG vibrational spectra observed in the O-H/N-H stretching region reveals that the free O-H stretching from the silanol groups on the silica surface at 3740 cm^{-1} is the predominant contribution to the bare quartz spectrum and is close to the 3750 cm^{-1} band assigned to the OH stretch of isolated silanols vibrating at the silica/air interface.[14, 97, 98] This sharp band is greatly suppressed with the increase surface coverage of the pesticide, similar to reports of hexane vapor,[99] atrazine, and ethylenediamine.[14, 91] The broad O-H stretching feature centered ~3500 cm^{-1} is consistent with a relatively large number of hydrogen bonded silanols at the solid/air interface.[69, 97, 98] Alternatively, it is possible that it could originate from loosely hydrogen-bonded water on the surface.[100]

After deposition, spectral features emerge in the 3300-3450 cm^{-1} region. We attribute these bands to the carbamate group N-H stretching since typical peptide NH stretch are reported in this region.[101-103] After spectral fitting to three Lorentzians according to **Equation 4**, we find a clearly resolved narrow peak at 3449 cm^{-1} that we tentatively assign as the "free" NH stretch and a broader dominant peak at 3328 cm^{-1} that we tentatively assign as hydrogen bonded NH groups.[104, 105] The two peaks are clearly of opposite phase and interfere with the very broad OH band centered ~3460 cm^{-1} (Figure 4C). It is important to note that the fitting yields only relative phase and not the absolute phase as in a heterodyned measurement. Another possible assignment may be overtones of the C=O stretching bands (*vide infra*) but they are expected to be much weaker contributions. The suppression of the silanol signals and the appearance of a carbaryl-based stretching bands suggests that carbaryl is physisorbed to silanol groups (and/or surface water). The role of hydrogen-bonding interactions between carbaryl NH group and the surface silanol/silanolates is proposed as follows: $\equiv SiOH\cdots NHR'COOR \Leftrightarrow \equiv SiO^{-}\cdots HN^{+}HR'COOR$; or $\equiv SiO^{-}\cdots HNR'COOR$ for silanols and silenolate groups, respectively. Siloxane bridges (Si–O–Si) may also act as a weak H-bond acceptors.[99]

C=O Stretching Region. ***Figure 5*** shows the spectra of carbaryl on silica in the C=O vibrational region with typical absorption in the 1600–1700 cm^{-1} range due to the carbamate ester group (O–C=O). For ester carbonyls, red shifted C=O bands are commonly attributed to stronger hydrogen bonding interactions.[106] Here, two dominant peaks with opposite phases are observed at 1699 and 1728 cm^{-1} as determined by the fitting of the experimental vSFG spectrum (***Figure 5***).

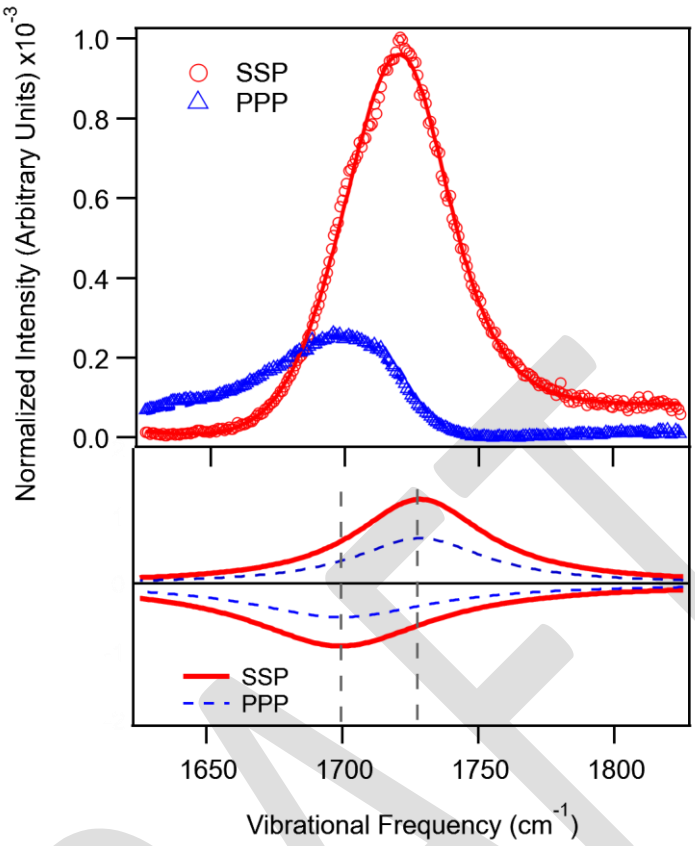

Figure 5. Representative CO vSFG spectra of carbaryl at the silica/air interface (top). The dots are the experimental data and the solid lines are the best fit results. The individual Lorentzians used in the fit are shown in the lower panel. Main spectral differences are due in part to a sign flip in the non-resonant response.

The higher frequency peak located at 1728 cm^{-1} could be assigned to a free C=O group not involved in hydrogen bonding with the N-H moiety serving as the anchor of the carbaryl adsorbate to silica as described above. The lower frequency peak at 1699 cm^{-1} is opposite in phase and suggests hydrogen bonding of the ester C=O groups to the silica O–H groups as ≡SiOH···OCORNHR'. We note that these two modes of binding are complementary to the amide NH stretch region (>3300 cm^{-1}). Both C=O and O-H/N–H bands are used to complement the results with the C–H stretching region by providing a full picture of intermolecular interactions at the interface.

MD Simulations. ***Figure 6C*** shows the joint probability distribution of orientations of the carbaryl molecule on amorphous silica, as described by molecular dynamics simulations (see SI for simulation details), as a function of the Euler tilt and twist angles, θ and ψ, respectively. Note

that the orientation of the naphthyl ring with respect to the surface can be described in terms of θ and ψ angles due to the planarity and rigidity of the carbaryl ring, defining the molecular orientation with respect to the laboratory frame (***Figure 6A***).

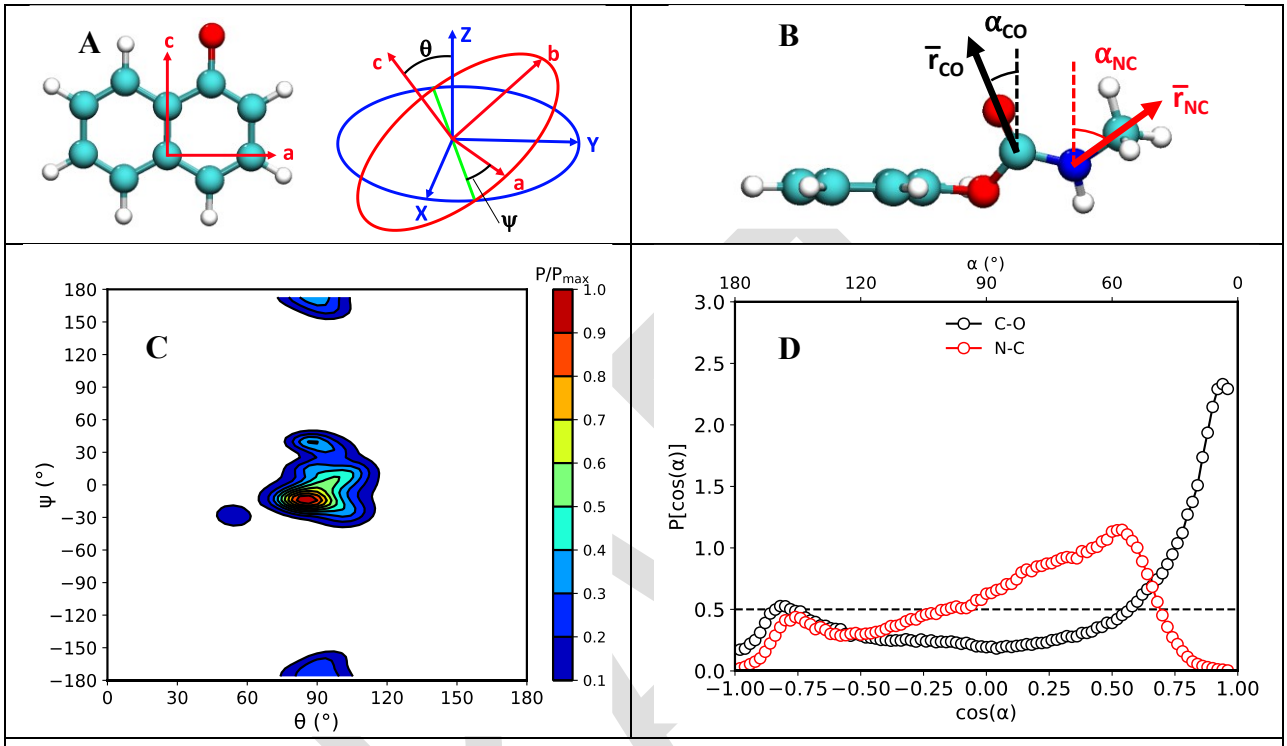

Figure 6. Carbaryl orientation on amorphous silica. **(A)** Definition of the molecular frame (a,b,c axis) and Euler tilt and twist angles (θ, ψ) used to characterize the orientation of the carbaryl's aromatic ring relative to the silica surface. Axes X,Y,Z represent the fixed laboratory frame on the silica surface, with Z normal to the interface. **(B)** Definition of the bond vectors and angles with respect to the surface normal, used to characterize the orientation of the carbamate group of carbaryl on silica. **(C)** Joint probability density $P(\theta, \psi)$ of finding the carbaryl molecule with Euler angles θ and ψ, normalized over its maximum P_{max}. **(D)** Probability density distribution of finding a carbaryl molecule with bond vector angles cos(α) with respect to the surface normal. Dashed lines correspond to an isotropic distribution of the angles.

The naphthyl distribution $P(\theta, \psi)$ in ***Figure 6C*** is characterized by broad and non-Gaussian distribution, peaked at $(86°, -15°)$, which correspond to the naphthyl aromatic ring oriented roughly parallel to the surface (***Figure 7*** shows representative configurations). We remark that an orientation with $(0°, 0°)$ and $(0°, \pm 180°)$ correspond to perfectly flat-lying aromatic ring with either one side or the other of the in contact with the surface. Note, however, that the naphthyl ring presents a broad distribution, spanning a range of configurations that represent non-flat

orientations (e.g., $\psi = \pm 30°$), reflecting the heterogeneity of the amorphous silica surface. The analysis of individual configurations along the MD trajectories shows that carbaryl molecules are kinetically trapped and do not sample the full range of possible orientations –*i.e.*, molecules starting on orientations with $\psi \approx 0°$ rarely convert to orientations with $\psi \approx \pm 180°$ and vice-versa (see SI), suggesting that interfacial interactions strongly stabilize the carbaryl on the silica surface (see below). However, each carbaryl molecule freely explore conformations involving both flat and non-flat orientations of the naphthyl ring on the picosecond time scale.

The joint probability distribution of Euler angles provides valuable information on the orientation of the aromatic ring but does not resolve the orientation of the flexible carbamate group, which can adopt a variety of conformations and orientations with respect to the aromatic ring. Therefore, we computed the angle between the surface normal and the carbonyl C=O bond vector (α_{CO}) and N-CH_3 bond vector (α_{NC}) to characterize the orientation of the carbamate group with respect to the interface (***Figure 6B***).

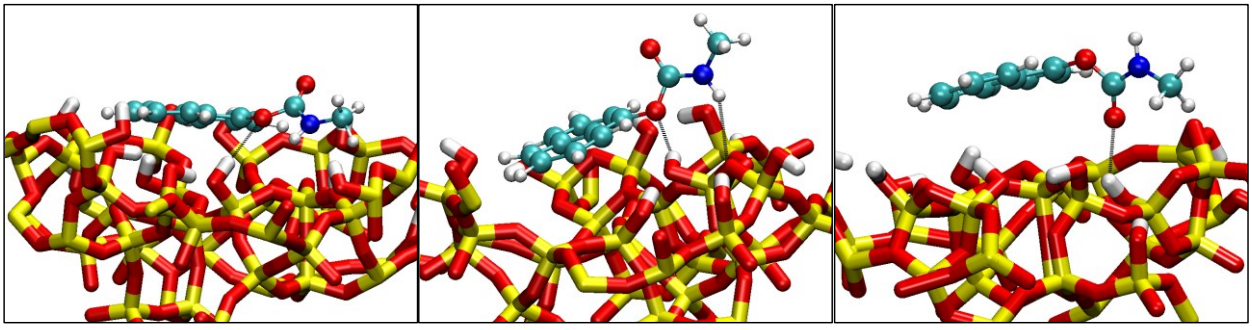

Figure 7. Typical configurations of the carbaryl molecule on the silica surface. Anchoring occurs primarily via hydrogen bonding interactions (black dot lines) between the surface silanols of the silica and the N-H/CO bond of the carbamate group within the pesticide. Orientations of the aromatic ring and CO and NC bonds of the pesticide with respect to the surface normal are indicated.

Figure 6D shows the probability distribution of the (cosine) angle between the CO and N-CH_3 bond vectors. The angle distributions are broad and non-Gaussian, highlighting the heterogeneity of the amorphous silica surface. The N-CH_3 group is characterized by a broad range of orientations, mostly spanning the 60°–90° range with an average angle of *ca.* 85° ($\langle \cos(\alpha_{NC}) \rangle = 0.1$). Correlated with this observation, the carbonyl distribution shows a localized peak at $\alpha_{CO} < 60°$,

corresponding to a population of *ca. 70% of molecules with the CO group pointing away from the surface and the NH group pointing toward the surface* (**Figure 7**, left and center). Analysis of the long tail of the carbonyl distribution also reveals *ca. 20% of configurations with the CO pointing into the surface* with $\alpha_{CO} > 120°$ (**Figure 7**, right). Representative snapshots from the molecular dynamic simulations reveal that H-bonding interactions with Si-OH groups on the silica surface stabilize those conformations, providing NH--O and OH--O anchoring groups for the carbaryl adsorbate (**Figure 7**). The analysis of the time-dependent evolution of the angles along the MD trajectories provides a dynamical picture of these H-bonding interactions (see SI). Interestingly, the carbaryl molecules explore the rough silica surface with no preferential orientation until an energetically favorable anchoring site is found that tightly binds the pesticide to the interface. The picture that emerges from the MD analysis suggests that carbaryl interacts with the silica surface primarily through the formation of hydrogen bonds between the O-H bond of the silanol groups and the NH/CO bond of the carbamate group with dominant configurations having the aromatic ring of the pesticide oriented roughly parallel to the silica surface and preferentially with the NH group pointing toward the surface.

SFG Simulations. Figure *8* shows the calculated SSP and PPP vSFG spectra obtained from the configurations of the MD simulations. SFG spectra were simulated at the DFT level as has been previously described (see SI for simulation details). [44-54] The SSP spectrum is characterized by three peaks corresponding to the CH_3(s) at ~2860 cm^{-1}, CH_3(FR) at 2960 cm^{-1} and aromatic ring C-H stretchings at ~3060 cm^{-1}, in excellent agreement with the experimental data. Upon PPP light polarization, the intensity of the symmetric CH_3 and high frequency aromatic signals diminish while the peaks corresponding to the antisymmetric CH_3 stretching at 2977 cm^{-1} dominate the spectra, in agreement with experimental observations. Therefore, the overall agreement between theory and experiments is quite satisfactory, supporting the predicted distribution of orientations of the carbaryl adsorbate on the silica surface.

A more detailed analysis of the SFG spectra reveals additional insights. First, we remark that the inclusion of Fermi resonances in the description of the spectra (which we include via an effective coupling Hamiltonian) is crucial to reproduce the experimental spectra (see Figure S8). In effect, SFG spectra computed at the harmonic level is not able to reproduce the low frequency peak. Second, giving the broad non-gaussian distributions of conformations that the carbamate group can adopt, we found that a single orientation is not sufficient for quantitative modeling of

the experimental spectrum. In effect, in **Figure 9** we present the calculated SSP and PPP vSFG spectra for two configurations representative of the 'up' and 'down' conformations that carbaryl adopt on the silica surface. Note that conformations for which the NH group is pointing toward or away from the surface give rise to SFG responses with different phases that, given the coherent nature of SFG spectroscopy, interfere to produce the final measured signal. Moreover, both SSP and PPP SFG signals are extremely sensible to the exact orientation of the ring with respect to the silica surface (see Figure S9). As such, the overall SFG signal results from a subtle phase cancelation that results from the Boltzmann average of configurations.

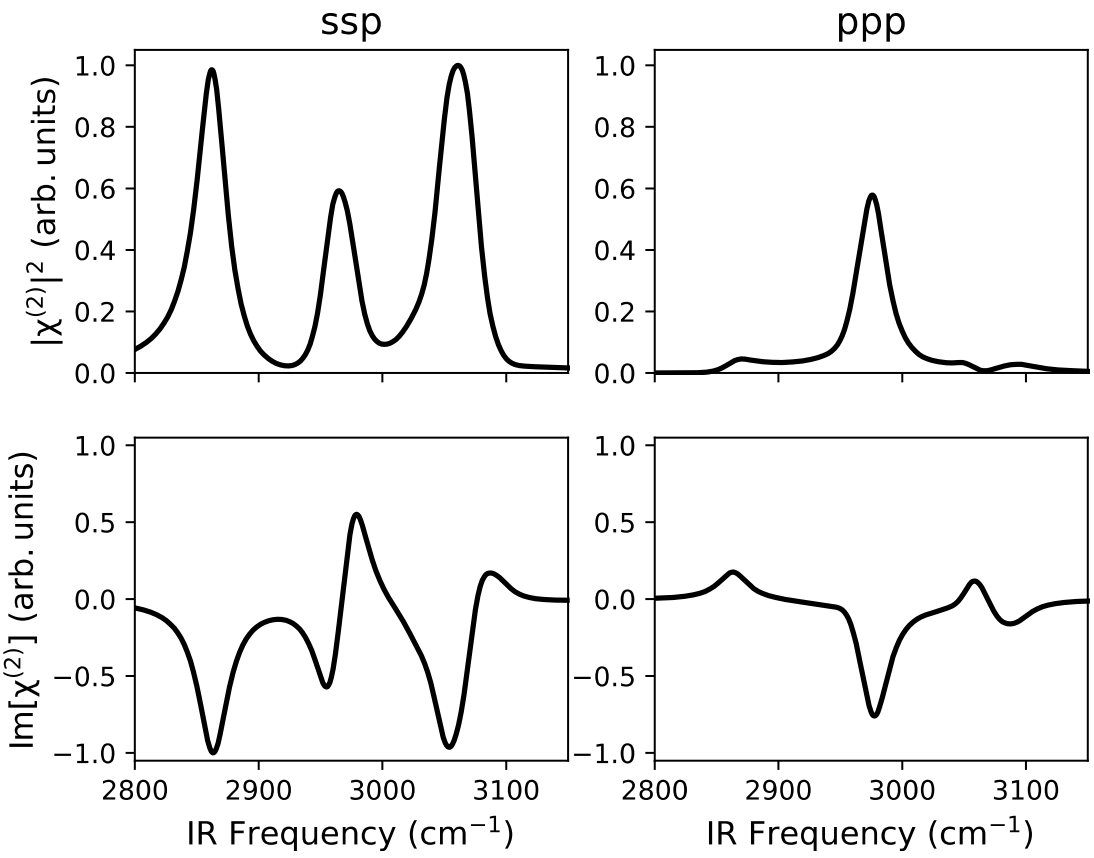

Figure 8. DFT-based SFG spectra of carbaryl on silica surface with SSP polarization and PPP polarization.

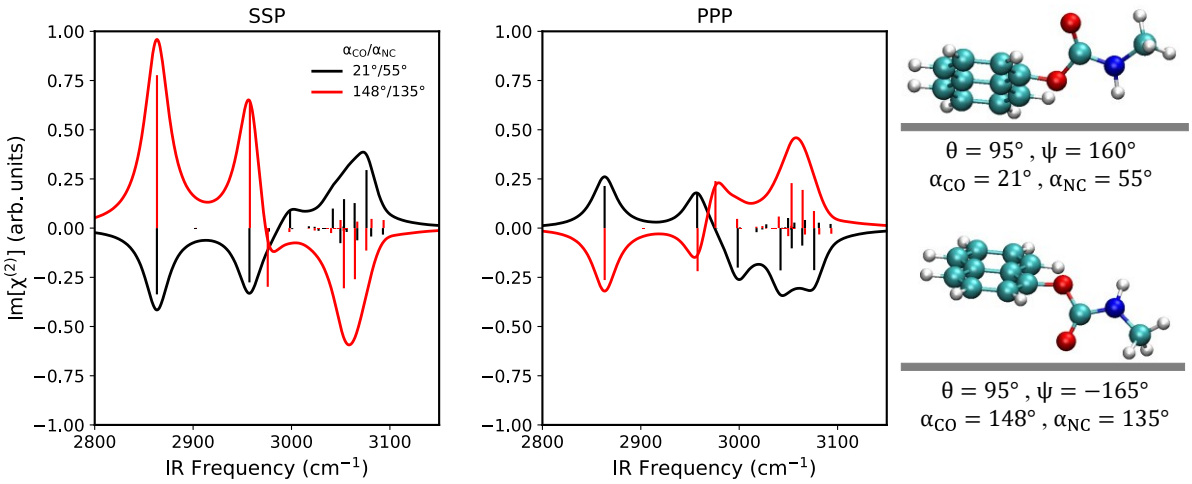

Figure 9. DFT-simulated SFG spectra of carbaryl with SSP (left) and PPP (right) polarization for specific orientations. Schematics of the orientations are shown on the right.

CONCLUSIONS

In summary, we have characterized the specific interactions responsible for the adsorption of carbaryl to silica surfaces. The carbaryl/silica interfacial system serves as a model for a variety of pesticides of environmental concern for which the interactions with silica surfaces remain to be understood at the molecular level. Carbaryl, as well as other carbamate pesticides, are ubiquitously employed in both private and commercial agriculture, and frequently interact with silica-rich media, such as soil particles and dust aerosols to produce a wide range of toxic substances. We have shown that vSFG in conjunction with computational modeling can provide a consistent characterization of the interfacial structure and binding motifs of carbaryl adsorbed on amorphous silica. We found evidence that carbaryl binds to silica surfaces primarily via hydrogen bonding interactions between the pesticide N-H/CO groups and the silanols of the silica surface. The distribution of configurations with the naphthyl group rougly parallel to the surface has been supported by both the molecular orientation derived from theoretical and SFG-VS data observed in the C-H stretching region, and directly observed in the SFG vibrational spectra collected in the N-H/C-O stretching region. The resulting insights are particularly valuable to better understand surface reactions of carbaryl pollutants under environmental conditions. In addition to providing

insights into an environmentally relevant system, our study demonstrates the effectiveness of a combined experimental and theoretical methodology which could be employed, more broadly, in the study of interactions between contaminants and diverse environmental surfaces.

ASSOCIATED CONTENT

Supporting Information

Detailed experimental methods, including description of sample preparation and instrumental details. Characterization data including Raman and FTIR results, and SFG curve fittings and analysis. Detailed computational methods, including description of molecular dynamic simulations, DFT calculations simulation of SFG spectroscopy.

ACKNOWLEDGMENTS

L.V. acknowledges support from the National Science Foundation (NSF) Grant # CHE-1610807 for this work. J.L.C.B thanks the Collaborative Learning and Integrated Mentoring in the Biosciences (CLIMB) program, supported by an award (GM 095459) from the National Institute of General Medical Science (National Institute of Health) to the State University of New York at Buffalo. V.S.B. acknowledges support from NSF Grant No. CHE-1900160 and high-performance computing time from the Yale High-Performance Computing Center. L.V. thanks Ning Dai (University at Buffalo) for valuable discussion on the topic of carbamate pesticides at interfaces.

REFERENCES

(1) Alavanja, M. C. R. Introduction: pesticides use and exposure extensive worldwide. *Rev. Environ. Health* **2009**, *24*, 303-309.
(2) Tankiewicz, M.; Fenik, J.; Biziuk, M. Determination of organophosphorus and organonitrogen pesticides in water samples. *TrAC, Trends Anal. Chem.* **2010**, *29*, 1050-1063.
(3) Jennings, A. A.; Li, Z. Worldwide regulatory guidance values applied to direct contact surface soil pesticide contamination: Part II—noncarcinogenic pesticides. *Air, Soil Water Res.* **2017**, *10*, 1-14.
(4) Jayaraj, R.; Megha, P.; Sreedev, P. Organochlorine pesticides, their toxic effects on living organisms and their fate in the environment. *Interdiscip. Toxicol.* **2016**, *9*, 90-100.
(5) Gilliom, R. J. Pesticides in U.S. Streams and Groundwater. *Environ. Sci. Technol.* **2007**, *41*, 3408-3414.

(6) Walters, J.; Goh, K. S.; Li, L.; Feng, H.; Hernandez, J.; White, J. Environmental monitoring of carbaryl applied in urban areas to control the glassy-winged sharpshooter in California. *Environ. Monit. Assess.* **2003**, *82*, 265-280.
(7) Demirbaş, A. Spectrophotometric determination of carbaryl pesticide and its hydrolysis product in soil and strawberry samples. *Sci. Total Environ.* **1998**, *220*, 235-241.
(8) Dennis, L. K.; Lynch, C. F.; Sandler, D. P.; Alavanja, M. C. R. Pesticide use and cutaneous melanoma in pesticide applicators in the agricultural heath study. *Environ. Health Perspect.* **2010**, *118*, 812-817.
(9) Fernandes de Oliveira, M.; Johnston, C. T.; Premachandra, G. S.; Teppen, B. J.; Li, H.; Laird, D. A.; Zhu, D.; Boyd, S. A. Spectroscopic Study of Carbaryl Sorption on Smectite from Aqueous Suspension. *Environ. Sci. Technol.* **2005**, *39*, 9123-9129.
(10) Hernández, A. F.; Parrón, T.; Tsatsakis, A. M.; Requena, M.; Alarcón, R.; López-Guarnido, O. Toxic effects of pesticide mixtures at a molecular level: their relevance to human health. *Toxicology* **2013**, *307*, 136-145.
(11) Lee, I.; Eriksson, P.; Fredriksson, A.; Buratovic, S.; Viberg, H. Developmental neurotoxic effects of two pesticides: Behavior and biomolecular studies on chlorpyrifos and carbaryl. *Toxicol. Appl. Pharmacol.* **2015**, *288*, 429-438.
(12) Aktar, M. W.; Sengupta, D.; Chowdhury, A. Impact of pesticides use in agriculture: their benefits and hazards. *Interdiscip. Toxicol.* **2009**, *2*, 1-12.
(13) Hancock, T. C.; Sandstrom, M. W.; Vogel, J. R.; Webb, R. M. T.; Bayless, E. R.; Barbash, J. E. Pesticide Fate and Transport throughout Unsaturated Zones in Five Agricultural Settings, USA. *J. Environ. Qual.* **2008**, *37*, 1086-1100.
(14) Casillas-Ituarte, N. N.; Allen, H. C. Water, chloroform, acetonitrile, and atrazine adsorption to the amorphous silica surface studied by vibrational sum frequency generation spectroscopy. *Chem. Phys. Lett.* **2009**, *483*, 84-89.
(15) Hromadová, M.; Sokolová, R.; Pospíšil, L.; Fanelli, N. Surface Interactions of s-Triazine-Type Pesticides. An Electrochemical Impedance Study. *J. Phys. Chem. B* **2006**, *110*, 4869-4874.
(16) Schrödle, S.; Richmond, G. L. In situ non-linear spectroscopic approaches to understanding adsorption at mineral–water interfaces. *J. Phys. D: Appl. Phys.* **2008**, *41*, 033001.
(17) Shirzadi, A.; Simpson, M. J.; Kumar, R.; Baer, A. J.; Xu, Y.; Simpson, A. J. Molecular Interactions of Pesticides at the Soil−Water Interface. *Environ. Sci. Technol.* **2008**, *42*, 5514-5520.
(18) Das, S. K.; Mukherjee, I.; Kumar, A. Effect of soil type and organic manure on adsorption–desorption of flubendiamide. *Environ. Monit. Assess.* **2015**, *187*, 403.
(19) Davies, J. E. D.; Jabeen, N. The Adsorption of Herbicides and Pesticides on Clay Minerals and Soils. Part 1. Isoproturon. *J. Inclusion Phenom. Macrocyclic Chem.* **2002**, *43*, 329-336.
(20) Huang, L.; Frank, E. S.; Shrestha, M.; Riahi, S.; Tobias, D. J.; Grassian, V. H. Heterogeneous interactions of prevalent indoor oxygenated organic compounds on hydroxylated SiO2 surfaces. *Environ. Sci. Technol.* **2021**, *55*, 6623-6630.
(21) Tubana, B. S.; Babu, T.; Datnoff, L. E. A Review of Silicon in Soils and Plants and Its Role in US Agriculture: History and Future Perspectives. *Soil Sci.* **2016**, *181*, 393-411.
(22) Siampiringue, M.; Chahboune, R.; Wong-Wah-Chung, P.; Sarakha, M. Carbaryl photochemical degradation on soil model surfaces. *Soil Syst.* **2019**, *3*, 17.
(23) Chen, W.; Long, F.; Song, G.; Chen, J.; Peng, S.; Li, P. Rapid and sensitive detection of pesticide residues using dynamic surface-enhanced Raman spectroscopy. *J. Raman Spectrosc.* **2020**, *51*, 611-618.

(24) Czaplicka, M.; Barchanska, H.; Jaworek, K.; Kaczmarczyk, B. The interaction between atrazine and the mineral horizon of soil: a spectroscopic study. *J. Soils Sediments* **2018**, *18*, 827-834.
(25) Ringwald, S. C.; Pemberton, J. E. Adsorption Interactions of Aromatics and Heteroaromatics with Hydrated and Dehydrated Silica Surfaces by Raman and FTIR Spectroscopies. *Environ. Sci. Technol.* **2000**, *34*, 259-265.
(26) Xu, M.-L.; Gao, Y.; Han, X. X.; Zhao, B. Detection of Pesticide Residues in Food Using Surface-Enhanced Raman Spectroscopy: A Review. *J. Agric. Food. Chem.* **2017**, *65*, 6719-6726.
(27) Chen, J.; Dong, D.; Ye, S. Detection of pesticide residue distribution on fruit surfaces using surface-enhanced Raman spectroscopy imaging. *RSC Advances* **2018**, *8*, 4726-4730.
(28) Bé, A. G.; Chase, H. M.; Liu, Y.; Upshur, M. A.; Zhang, Y.; Tuladhar, A.; Chase, Z. A.; Bellcross, A. D.; Wang, H.-F.; Wang, Z.; et al. Atmospheric β-Caryophyllene-Derived Ozonolysis Products at Interfaces. *ACS Earth Space Chem.* **2019**, *3*, 158-169.
(29) Covert, P. A.; Hore, D. K. Geochemical Insight from Nonlinear Optical Studies of Mineral–Water Interfaces. *Annu. Rev. Phys. Chem.* **2016**, *67*, 233-257.
(30) Lambert, A. G.; Davies, P. B.; Neivandt, D. J. Implementing the Theory of Sum Frequency Generation Vibrational Spectroscopy: A Tutorial Review. *Appl. Spectrosc. Rev.* **2005**, *40*, 103-145.
(31) Liu, A.; Huang, Z.; Deng, G.; Guo, Y. Adsorption of benzonitrile at the air/water interface studied by sum frequency generation spectroscopy. *Chin. Sci. Bull.* **2013**, *58*, 1529-1535.
(32) Ohno, P. E.; Saslow, S. A.; Wang, H.-f.; Geiger, F. M.; Eisenthal, K. B. Phase-referenced nonlinear spectroscopy of the α-quartz/water interface. *Nat. Commun.* **2016**, *7*, 13587.
(33) Bui, T. T.; Colón, L. A.; Velarde, L. Intermolecular Interactions at the Silica–Liquid Interface Modulate the Fermi Resonance Coupling in Surface Methanol. *J. Phys. Chem. Lett.* **2021**, *12*, 5695-5702.
(34) Wang, H.-F.; Velarde, L.; Gan, W.; Fu, L. Quantitative Sum-Frequency Generation Vibrational Spectroscopy of Molecular Surfaces and Interfaces: Lineshape, Polarization, and Orientation. *Annu. Rev. Phys. Chem.* **2015**, *66*, 189-216.
(35) Das, S. K.; Sengupta, S.; Velarde, L. Interfacial surfactant ordering in thin films of SDS-encapsulated single-walled carbon nanotubes. *J. Phys. Chem. Lett.* **2016**, *7*, 320-326.
(36) Chase, H. M.; Rudshteyn, B.; Psciuk, B. T.; Upshur, M. A.; Strick, B. F.; Thomson, R. J.; Batista, V. S.; Geiger, F. M. Assessment of DFT for Computing Sum Frequency Generation Spectra of an Epoxydiol and a Deuterated Isotopologue at Fused Silica/Vapor Interfaces. *J. Phys. Chem. B* **2016**, *120*, 1919-1927.
(37) Ebben, C. J.; Ault, A. P.; Ruppel, M. J.; Ryder, O. S.; Bertram, T. H.; Grassian, V. H.; Prather, K. A.; Geiger, F. M. Size-Resolved Sea Spray Aerosol Particles Studied by Vibrational Sum Frequency Generation. *J. Phys. Chem. A* **2013**, *117*, 6589-6601.
(38) Fairbrother, D. H.; Geiger, F. M. Environmental Processes at the Solid–Liquid Interface: What Constitutes New Physical Insights? *J. Phys. Chem. A* **2017**, *121*, 5947-5947.
(39) Jubb, A. M.; Hua, W.; Allen, H. C. Environmental chemistry at vapor/water interfaces: insights from vibrational sum frequency generation spectroscopy. *Annu. Rev. Phys. Chem.* **2012**, *63*, 107-130.
(40) Avery, C. W.; Som, A.; Xu, Y.; Tew, G. N.; Chen, Z. Dependence of antimicrobial selectivity and potency on oligomer structure investigated using substrate supported lipid bilayers and sum frequency generation vibrational spectroscopy. *Anal. Chem.* **2009**, *81*, 8365-8372.

(41) Li, Y.; Wei, S.; Wu, J.; Jasensky, J.; Xi, C.; Li, H.; Xu, Y.; Wang, Q.; Marsh, E. N. G.; Brooks III, C. L. Effects of peptide immobilization sites on the structure and activity of surface-tethered antimicrobial peptides. *J. Phys. Chem. C* **2015**, *119*, 7146-7155.
(42) Xiao, M.; Jasensky, J.; Foster, L.; Kuroda, K.; Chen, Z. Monitoring antimicrobial mechanisms of surface-immobilized peptides in situ. *Langmuir* **2018**, *34*, 2057-2062.
(43) Ye, S.; Majumdar, P.; Chisholm, B.; Stafslien, S.; Chen, Z. Antifouling and antimicrobial mechanism of tethered quaternary ammonium salts in a cross-linked poly (dimethylsiloxane) matrix studied using sum frequency generation vibrational spectroscopy. *Langmuir* **2010**, *26*, 16455-16462.
(44) Anfuso, C. L.; Snoeberger, R. C.; Ricks, A. M.; Liu, W.; Xiao, D.; Batista, V. S.; Lian, T. Covalent Attachment of a Rhenium Bipyridyl CO_2 Reduction Catalyst to Rutile TiO_2. *J. Am. Chem. Soc.* **2011**, *133*, 6922-6925.
(45) Anfuso, C. L.; Xiao, D.; Ricks, A. M.; Negre, C. F. A.; Batista, V. S.; Lian, T. Orientation of a Series of CO_2 Reduction Catalysts on Single Crystal TiO_2 Probed by Phase-Sensitive Vibrational Sum Frequency Generation Spectroscopy (PS-VSFG). *J. Phys. Chem. C* **2012**, *116*, 24107-24114.
(46) Cattaneo, M.; Guo, F.; Kelly, H. R.; Videla, P. E.; Kiefer, L.; Gebre, S.; Ge, A.; Liu, Q.; Wu, S.; Lian, T.; et al. Robust Binding of Disulfide-Substituted Rhenium Bipyridyl Complexes for CO_2 Reduction on Gold Electrodes. *Front. Chem.* **2020**, *8*, 86.
(47) Clark, M. L.; Ge, A.; Videla, P. E.; Rudshteyn, B.; Miller, C. J.; Song, J.; Batista, V. S.; Lian, T.; Kubiak, C. P. CO_2 Reduction Catalysts on Gold Electrode Surfaces Influenced by Large Electric Fields. *J. Am. Chem. Soc.* **2018**, *140*, 17643-17655.
(48) Clark, M. L.; Rudshteyn, B.; Ge, A.; Chabolla, S. A.; Machan, C. W.; Psciuk, B. T.; Song, J.; Canzi, G.; Lian, T.; Batista, V. S.; et al. Orientation of Cyano-Substituted Bipyridine Re(I) fac-Tricarbonyl Electrocatalysts Bound to Conducting Au Surfaces. *J. Phys. Chem. C* **2016**, *120*, 1657-1665.
(49) Ge, A.; Rudshteyn, B.; Psciuk, B. T.; Xiao, D.; Song, J.; Anfuso, C. L.; Ricks, A. M.; Batista, V. S.; Lian, T. Surface-Induced Anisotropic Binding of a Rhenium CO_2-Reduction Catalyst on Rutile TiO_2(110) Surfaces. *J. Phys. Chem. C* **2016**, *120*, 20970-20977.
(50) Ge, A.; Rudshteyn, B.; Videla, P. E.; Miller, C. J.; Kubiak, C. P.; Batista, V. S.; Lian, T. Heterogenized Molecular Catalysts: Vibrational Sum-Frequency Spectroscopic, Electrochemical, and Theoretical Investigations. *Acc. Chem. Res.* **2019**, *52*, 1289-1300.
(51) Ge, A.; Videla, P. E.; Lee, G. L.; Rudshteyn, B.; Song, J.; Kubiak, C. P.; Batista, V. S.; Lian, T. Interfacial Structure and Electric Field Probed by in Situ Electrochemical Vibrational Stark Effect Spectroscopy and Computational Modeling. *J. Phys. Chem. C* **2017**, *121*, 18674-18682.
(52) Ge, A.; Videla, P. E.; Rudshteyn, B.; Liu, Q.; Batista, V. S.; Lian, T. Dopant-Dependent SFG Response of Rhenium CO_2 Reduction Catalysts Chemisorbed on $SrTiO_3$ (100) Single Crystals. *J. Phys. Chem. C* **2018**, *122*, 13944-13952.
(53) Ho, J.; Psciuk, B. T.; Chase, H. M.; Rudshteyn, B.; Upshur, M. A.; Fu, L.; Thomson, R. J.; Wang, H.-F.; Geiger, F. M.; Batista, V. S. Sum Frequency Generation Spectroscopy and Molecular Dynamics Simulations Reveal a Rotationally Fluid Adsorption State of α-Pinene on Silica. *J. Phys. Chem. C* **2016**, *120*, 12578-12589.
(54) Mifflin, A. L.; Velarde, L.; Ho, J.; Psciuk, B. T.; Negre, C. F. A.; Ebben, C. J.; Upshur, M. A.; Lu, Z.; Strick, B. L.; Thomson, R. J.; et al. Accurate Line Shapes from Sub-1 cm^{-1}

Resolution Sum Frequency Generation Vibrational Spectroscopy of α-Pinene at Room Temperature. *J. Phys. Chem. A* **2015**, *119*, 1292-1302.
(55) Shen, Y. Phase-sensitive sum-frequency spectroscopy. *Annu. Rev. Phys. Chem.* **2013**, *64*, 129-150.
(56) Wang, H.-F. Sum frequency generation vibrational spectroscopy (SFG-VS) for complex molecular surfaces and interfaces: Spectral lineshape measurement and analysis plus some controversial issues. *Prog. Surf. Sci.* **2016**, *91*, 155-182.
(57) Zhu, X. D.; Suhr, H.; Shen, Y. R. Surface vibrational spectroscopy by infrared-visible sum frequency generation. *Phys. Rev. B* **1987**, *35*, 3047-3050.
(58) Wang , H.-F.; Gan, W.; Lu, R.; Rao, Y.; Wu, B.-H. Quantitative spectral and orientational analysis in surface sum frequency generation vibrational spectroscopy (SFG-VS). *Int. Rev. Phys. Chem.* **2005**, *24*, 191-256.
(59) Ye, S.; Nihonyanagi, S.; Uosaki, K. Sum frequency generation (SFG) study of the pH-dependent water structure on a fused quartz surface modified by an octadecyltrichlorosilane (OTS) monolayer. *Phys. Chem. Chem. Phys.* **2001**, *3*, 3463-3469.
(60) Richter, L. J.; Petralli-Mallow, T. P.; Stephenson, J. C. Vibrationally resolved sum-frequency generation with broad-bandwidth infrared pulses. *Opt. Lett.* **1998**, *23*, 1594-1596.
(61) Algoul, S. T.; Sengupta, S.; Bui, T. T.; Velarde, L. Tuning the Surface Ordering of Self-Assembled Ionic Surfactants on Semiconducting Single-Walled Carbon Nanotubes: Concentration, Tube Diameter, and Counterions. *Langmuir* **2018**, *34*, 9279-9288.
(62) Elsenbeck, D.; Das, S. K.; Velarde, L. Substrate influence on the interlayer electron–phonon couplings in fullerene films probed with doubly-resonant SFG spectroscopy. *Phys. Chem. Chem. Phys.* **2017**, *19*, 18519-18528.
(63) Kearns, H.; Sengupta, S.; Sasselli, I. R.; Bromley Iii, L.; Faulds, K.; Tuttle, T.; Bedics, M. A.; Detty, M. R.; Velarde, L.; Graham, D.; et al. Elucidation of the bonding of a near infrared dye to hollow gold nanospheres - a chalcogen tripod. *Chem. Sci.* **2016**, *7*, 5160-5170.
(64) Sengupta, S.; Bromley Iii, L.; Velarde, L. Aggregated States of Chalcogenorhodamine Dyes on Nanocrystalline Titania Revealed by Doubly Resonant Sum Frequency Spectroscopy. *J. Phys. Chem. C* **2017**, *121*, 3424-3436.
(65) Fu, L.; Chen, S.-L.; Wang, H.-F. Validation of Spectra and Phase in Sub-1 cm^{-1} Resolution Sum-Frequency Generation Vibrational Spectroscopy through Internal Heterodyne Phase-Resolved Measurement. *J. Phys. Chem. B* **2016**, *120*, 1579-1589.
(66) Hu, X.-H.; Wei, F.; Wang, H.; Wang, H.-F. α-quartz crystal as absolute intensity and phase standard in sum-frequency generation vibrational spectroscopy. *J. Phys. Chem. C* **2019**, *123*, 15071-15086.
(67) Chase, H. M.; Ho, J.; Upshur, M. A.; Thomson, R. J.; Batista, V. S.; Geiger, F. M. Unanticipated Stickiness of α-Pinene. *J. Phys. Chem. A* **2017**, *121*, 3239-3246.
(68) Cruz-Chu, E. R.; Aksimentiev, A.; Schulten, K. Water−Silica Force Field for Simulating Nanodevices. *J. Phys. Chem. B* **2006**, *110*, 21497-21508.
(69) Zhuravlev, L. T. The surface chemistry of amorphous silica. Zhuravlev model. *Colloids Surf., A* **2000**, *173*, 1-38.
(70) Leroch, S.; Wendland, M. Simulation of Forces between Humid Amorphous Silica Surfaces: A Comparison of Empirical Atomistic Force Fields. *J. Phys. Chem. C* **2012**, *116*, 26247-26261.
(71) Skelton, A. A.; Fenter, P.; Kubicki, J. D.; Wesolowski, D. J.; Cummings, P. T. Simulations of the Quartz(10$\bar{1}$1)/Water Interface: A Comparison of Classical Force Fields, Ab Initio

Molecular Dynamics, and X-ray Reflectivity Experiments. *J. Phys. Chem. C* **2011**, *115*, 2076-2088.
(72) Lorenz, C. D.; Crozier, P. S.; Anderson, J. A.; Travesset, A. Molecular Dynamics of Ionic Transport and Electrokinetic Effects in Realistic Silica Channels. *J. Phys. Chem. C* **2008**, *112*, 10222-10232.
(73) Yesselman, J. D.; Price, D. J.; Knight, J. L.; Brooks Iii, C. L. MATCH: An atom-typing toolset for molecular mechanics force fields. *J. Comput. Chem.* **2012**, *33*, 189-202.
(74) Vanommeslaeghe, K.; Hatcher, E.; Acharya, C.; Kundu, S.; Zhong, S.; Shim, J.; Darian, E.; Guvench, O.; Lopes, P.; Vorobyov, I.; et al. CHARMM general force field: A force field for drug-like molecules compatible with the CHARMM all-atom additive biological force fields. *J. Comput. Chem.* **2010**, *31*, 671-690.
(75) Vanommeslaeghe, K.; MacKerell, A. D. Automation of the CHARMM General Force Field (CGenFF) I: Bond Perception and Atom Typing. *J. Chem. Inf. Model.* **2012**, *52*, 3144-3154.
(76) Vanommeslaeghe, K.; Raman, E. P.; MacKerell, A. D. Automation of the CHARMM General Force Field (CGenFF) II: Assignment of Bonded Parameters and Partial Atomic Charges. *J. Chem. Inf. Model.* **2012**, *52*, 3155-3168.
(77) Becke, A. D. Density-functional thermochemistry. III. The role of exact exchange. *J. Chem. Phys.* **1993**, *98*, 5648-5652.
(78) Frisch, M. J.; Pople, J. A.; Binkley, J. S. Self-consistent molecular orbital methods 25. Supplementary functions for Gaussian basis sets. *J. Chem. Phys.* **1984**, *80*, 3265-3269.
(79) Hariharan, P. C.; Pople, J. A. The influence of polarization functions on molecular orbital hydrogenation energies. *Theor. Chim. Acta* **1973**, *28*, 213-222.
(80) Phillips, J. C.; Braun, R.; Wang, W.; Gumbart, J.; Tajkhorshid, E.; Villa, E.; Chipot, C.; Skeel, R. D.; Kalé, L.; Schulten, K. Scalable molecular dynamics with NAMD. *J. Comput. Chem.* **2005**, *26*, 1781-1802.
(81) Martínez, L.; Andrade, R.; Birgin, E. G.; Martínez, J. M. PACKMOL: A package for building initial configurations for molecular dynamics simulations. *J. Comput. Chem.* **2009**, *30*, 2157-2164.
(82) Frisch, M. J.; Trucks, G. W.; Schlegel, H. B.; Scuseria, G. E.; Robb, M. A.; Cheeseman, J. R.; Scalmani, G.; Barone, V.; Petersson, G. A.; Nakatsuji, H.; et al. Gaussian 09, rev. D.01: Gaussian, I., Wallingford CT, 2016.
(83) Barone, V.; Bloino, J.; Guido, C. A.; Lipparini, F. A fully automated implementation of VPT2 Infrared intensities. *Chem. Phys. Lett.* **2010**, *496*, 157-161.
(84) Biczysko, M.; Bloino, J.; Carnimeo, I.; Panek, P.; Barone, V. Fully ab initio IR spectra for complex molecular systems from perturbative vibrational approaches: Glycine as a test case. *J. Mol. Struct.* **2012**, *1009*, 74-82.
(85) Bloino, J.; Barone, V. A second-order perturbation theory route to vibrational averages and transition properties of molecules: General formulation and application to infrared and vibrational circular dichroism spectroscopies. *J. Chem. Phys.* **2012**, *136*, 124108.
(86) Yagi, K.; Hirata, S.; Hirao, K. Vibrational quasi-degenerate perturbation theory: applications to fermi resonance in CO_2, H_2CO, and C_6H_6. *Phys. Chem. Chem. Phys.* **2008**, *10*, 1781-1788.
(87) Yan, E. C. Y.; Fu, L.; Wang, Z.; Liu, W. Biological Macromolecules at Interfaces Probed by Chiral Vibrational Sum Frequency Generation Spectroscopy. *Chem. Rev.* **2014**, *114*, 8471-8498.
(88) Zhuang, X.; Miranda, P. B.; Kim, D.; Shen, Y. R. Mapping molecular orientation and conformation at interfaces by surface nonlinear optics. *Phys. Rev. B* **1999**, *59*, 12632-12640.

(89) Hommel, E. L.; Allen, H. C. The air–liquid interface of benzene, toluene, m-xylene, and mesitylene: a sum frequency, Raman, and infrared spectroscopic study. *Analyst* **2003**, *128*, 750-755.
(90) Quast, A. D.; Wilde, N. C.; Matthews, S. S.; Maughan, S. T.; Castle, S. L.; Patterson, J. E. Improved assignment of vibrational modes in sum-frequency spectra in the CH stretch region for surface-bound C_{18} alkylsilanes. *Vib. Spectrosc* **2012**, *61*, 17-24.
(91) Xu, M.; Liu, D.; Allen, H. C. Ethylenediamine at Air/Liquid and Air/Silica Interfaces: Protonation Versus Hydrogen Bonding Investigated by Sum Frequency Generation Spectroscopy. *Environ. Sci. Technol.* **2006**, *40*, 1566-1572.
(92) Hommel, E. L.; Allen, H. C. 1-methyl naphthalene reorientation at the air− liquid interface upon water saturation studied by vibrational broad bandwidth sum frequency generation spectroscopy. *J. Phys. Chem. B* **2003**, *107*, 10823-10828.
(93) Marks, K.; Yazdi, M. G.; Piskorz, W.; Simonov, K.; Stefanuik, R.; Sostina, D.; Guarnaccio, A.; Ovsyannikov, R.; Giangrisostomi, E.; Sassa, Y. Investigation of the surface species during temperature dependent dehydrogenation of naphthalene on Ni (111). *J. Chem. Phys.* **2019**, *150*, 244704.
(94) Himmelhaus, M.; Eisert, F.; Buck, M.; Grunze, M. Self-Assembly of n-Alkanethiol Monolayers. A Study by IR−Visible Sum Frequency Spectroscopy (SFG). *J. Phys. Chem. B* **2000**, *104*, 576-584.
(95) Ji, N.; Ostroverkhov, V.; Chen, C.-Y.; Shen, Y.-R. Phase-Sensitive Sum-Frequency Vibrational Spectroscopy and Its Application to Studies of Interfacial Alkyl Chains. *J. Am. Chem. Soc.* **2007**, *129*, 10056-10057.
(96) Rocha-Mendoza, I.; Yankelevich, D. R.; Wang, M.; Reiser, K. M.; Frank, C. W.; Knoesen, A. Sum frequency vibrational spectroscopy: the molecular origins of the optical second-order nonlinearity of collagen. *Biophys. J.* **2007**, *93*, 4433-4444.
(97) Dalstein, L.; Potapova, E.; Tyrode, E. The elusive silica/water interface: Isolated silanols under water as revealed by vibrational sum frequency spectroscopy. *Phys. Chem. Chem. Phys.* **2017**, *19*, 10343-10349.
(98) Zhdanov, S.; Kosheleva, L.; Titova, T. IR study of hydroxylated silica. *Langmuir* **1987**, *3*, 960-967.
(99) Isaienko, O.; Borguet, E. Hydrophobicity of hydroxylated amorphous fused silica surfaces. *Langmuir* **2013**, *29*, 7885-7895.
(100) Backus, E. H.; Schaefer, J.; Bonn, M. Probing the mineral–water interface with nonlinear optical spectroscopy. *Angew. Chem. Int. Ed.* **2021**, *60*, 10482-10501.
(101) Chen, X.; Sagle, L. B.; Cremer, P. S. Urea orientation at protein surfaces. *J. Am. Chem. Soc.* **2007**, *129*, 15104-15105.
(102) Weidner, T.; Breen, N. F.; Drobny, G. P.; Castner, D. G. Amide or amine: determining the origin of the 3300 cm^{-1} NH mode in protein SFG spectra using ^{15}N isotope labels. *J. Phys. Chem. B* **2009**, *113*, 15423-15426.
(103) Konstantinovsky, D.; Perets, E. A.; Santiago, T.; Velarde, L.; Hammes-Schiffer, S.; Yan, E. C. Detecting the First Hydration Shell Structure around Biomolecules at Interfaces. *ACS Cent. Sci.* **2022**, *8*, 1404-1414.
(104) Bacsik, Z.; Atluri, R.; Garcia-Bennett, A. E.; Hedin, N. Temperature-induced uptake of CO_2 and formation of carbamates in mesocaged silica modified with n-propylamines. *Langmuir* **2010**, *26*, 10013-10024.

(105) Bonora, G. M.; Mapelli, C.; Toniolo, C.; Wilkening, R. R.; Stevens, E. S. Conformational analysis of linear peptides: 5. Spectroscopic characterization of β-turns in Aib-containing oligopeptides in chloroform. *Int. J. Biol. Macromol.* **1984**, *6*, 179-188.
(106) Blume, A.; Hübner, W.; Messner, G. Fourier transform infrared spectroscopy of $^{13}C=O$ labeled phospholipids hydrogen bonding to carbonyl groups. *Biochemistry* **1988**, *27*, 8239-8249.